Chapter 4.

Power dependent Raman spectra, nitrogen adsorption-desorption isotherms, and photocatalytic activity of WS_2 nanosystems exposed to UV- and β-radiation

4.1 Introduction

The organic and inorganic pollutants found in industrial wastewater have posed significant health risks, especially in developing countries, in recent decades. The textile and paper industries use vast quantities of organic dyes and synthetic pigments, leading to severe environmental issues. Synthetic dyes are commonly employed in industries such as textiles, leather, cosmetics, and pulp and paper, resulting in the disposal of alarming amounts of coloured organic dyes. These dye residues are highly carcinogenic, and a significant portion (1% -10%) of the dye is wasted during the product dyeing process, eventually ending up in wastewater. Specifically, azo dyes are the primary constituents of wastewater from textile industries and processing units [1,2].

Two-dimensional (2D) transition metal dichalcogenides (TMDCs) have gained considerable attention as photocatalysts due to their strong light absorption, remarkable chemical stability, and cost-effectiveness. These materials have been widely employed in pollutant removal [3,4]. It is well established that the edge sites of TMDCs play a crucial role in catalytic applications, as they provide active surface sites, while the basal plane remains relatively inert [5]. Additionally, radiation-based modifications using radionuclides have emerged as a valuable and cost-effective approach for enhancing the properties of TMDC materials [6]. Specifically, exposure to charged particle ions, energetic electrons, and γ-rays induces chalcogen vacancy-related point defects within TMDCs, inducing observable modification to the material properties at large. Furthermore, the microporous nature of 2D TMDC materials has demonstrated immense potential in hydrogen evolution reaction, photocatalysis, and electrocatalysis, along with nonlinear light absorption capabilities [7]. One of the effective strategies for improving nanomaterial performance is exploiting porous 2D layered structures. These hierarchical 2D materials exhibit superior physical and chemical properties due to their distinctive structural and morphological advantages. These porous hierarchical materials exhibit multiple ranges of porosity across different length scales, including (i) micropores (dia. <2 nm), (ii) mesopores (dia. ~2-50 nm), and (iii) macropores (dia. >50 nm) [8]. These materials also exhibit bimodal pore distributions, such as (i) micro-meso, (ii) meso-macro, and (iii) micro-macro, as well as trimodal distributions encompassing micro-to-macro and meso-to-macro pores. The ability to control pore size distribution is particularly significant for applications requiring specific functionalities [9,10]. According to reports, microporous

structures effectively harness visible light due to their increased surface area, which enhances photo-induced electron transfer. This, in line, leads to improved photocatalytic performance [11,12].

This chapter examines the impact of radiation exposure on layered WS_2 systems using (UV) and beta (β) rays. Irradiation on WS_2 systems is employed to develop a porous structure with diverse micro- and mesopores. Furthermore, the effect of these porous structures on the photocatalytic dye degradation activity of congo red, an azo dye, was investigated using irradiated WS_2 systems as a nano-catalyst.

4.2 Irradiation of WS_2 system with UV- and β-rays

The exfoliated WS_2 powder was subjected to irradiation utilising UV- and β-rays. For this process, 1.5 g of exfoliated WS_2 material was evenly spread onto microscope glass slides for each experimental condition. One of these slides was placed inside a UV chamber, positioned 12 cm below a UV lamp offering excitation wavelength, λ_{ex} = 365 nm, with an intensity of ~ 800 $\mu W/cm^2$ and exposed for a time duration of ~30 min. Similarly, another 1.5 g sample of exfoliated WS_2 powder was irradiated with β-rays inside a Pb-shielded chamber. A laboratory-grade ^{137}Cs source was employed to emit β-radiation, transitioning through a metastable energy state of ~0.51 MeV and a stable state near ~1.17 MeV, delivering a total radiation dose of 0.2 kGy (shown in *Appendix* (Fig. A2)) [13]. All irradiation procedures were conducted at room temperature (300 K).

4.3 Execution of photocatalytic experiment

The photocatalytic activity was evaluated using commercially available congo red (CR) dye (ACS reagent, Himedia®) as the target material. Photocatalytic experiments were conducted on three different samples, specifically exfoliated WS_2, UV-irradiated WS_2, and β-irradiated WS_2. To prepare the stock solution, 25 mg/L of CR dye was mixed in a borosil beaker, and 125 mg/L of exfoliated WS_2 was added as a photocatalyst. The mixture was stirred using a magnetic stirrer at room temperature in complete darkness for ~1 h to achieve adsorption-desorption equilibrium. Similarly, CR dye solutions with UV- and β-irradiated WS_2 catalysts were prepared to assess their photocatalytic degradation efficiency. The prepared solutions were placed inside a UV chamber, with the light source being positioned 12 cm above the specimen under study. The exfoliated WS_2 sample was exposed for approximately 75 min, while the irradiated WS_2 samples were exposed for a

time duration of ~45 min. At an interval of 15 min, 3 mL of the solution was collected in a quartz cuvette to measure the absorbance spectra. The degradation percentage of the dye was calculated using the popular formula [14],

$$\%\ degradation = \left(1 - \frac{C}{C_0}\right) \times 100 = \left(1 - \frac{A}{A_0}\right) \times 100 \quad (4.1)$$

where C_0 and C represent the concentration of CR dye at an initial time (0 min) and time t, respectively, while A_0 and A correspond to the strength of the maximum peak in the recorded absorbance spectra.

4.4. Morphological and elemental analysis

The surface morphologies of bulk WS_2, exfoliated WS_2, and systems subjected to UV- and β-irradiation are analysed with the help of captured FE-SEM images, depicted in Fig. 4.1(a-d). The bulk WS_2 appears as thick, agglomerated stacks of layers. In contrast, exfoliated WS_2 and irradiated systems exhibit a distinct separation of thin sheets while preserving

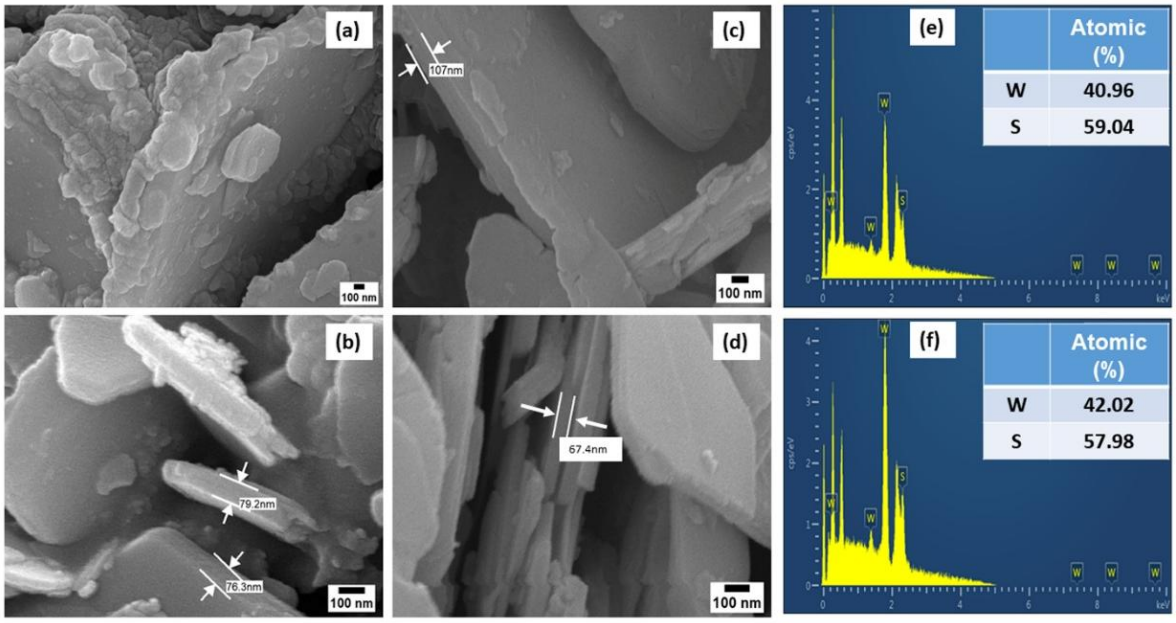

Figure 4.1: FE-SEM images of (a) bulk WS_2, (b) exfoliated WS_2, (c) UV-irradiated WS_2 and (d) β-irradiated WS_2 at lower magnifications (scale bar: 100 nm) respectively can be seen, while higher magnifications of the respective systems are shown in the right corner of the figures as insets; (e, f) EDX spectra of UV- and β-irradiated WS_2 systems.

their layered nature. Notably, some fragmented or uneven segments may have formed due to the shear forces acting on the sheets during prolonged irradiation. Elemental analysis of the irradiated systems, as shown in Fig. 4.1(e, f), revealed sulfur vacancies caused by exposure to UV and β-rays. By calculating the sulfur to tungsten (S/W) ratio from EDX spectra of scanned areas, a further decline in the stoichiometric ratio of WS_2 was observed, reaching a W:S ratio of 1:1.44 for UV exposure and 1:1.38 for β-ray exposure cases. The decrease in the number of sulfur atoms in the WS_2 system after β-irradiation is attributed to the much higher energy of beta particles, which can remove a larger number of sulfur atoms than the lower-energy UV irradiation.

4.5. Laser power-dependent Raman analysis

Raman spectra were obtained for bulk WS_2, exfoliated WS_2, and UV- and β-irradiated WS_2 systems, as shown in Fig. 4.2(a). The two most prominent peaks correspond to the vibrational mode observed at ~351 cm^{-1}, which emerges from the strong covalent bonding between S and W atoms, while the out-of-plane mode, at ~421 cm^{-1}, corresponds to vibrations amongst layers of S atoms linked through van der Waals bonding. Additionally, poorly resolved second-order or mixed modes were located at ~523 cm^{-1} and ~583 cm^{-1}, which are attributed to the $E^1_{2g} + LA$ and $A_{1g} + LA$ modes, respectively [15]. Deconvoluted spectra of the WS_2 system after β-irradiation is shown in the *Appendix* (Fig. A3). A noticeable redshift and broadening of these peaks, associated with both in-plane and out-of-plane vibrational modes, suggest a reduction in the number of layers after exfoliation compared to the pristine structure. This can be realized from an increase in the intensity ratio of E^1_{2g}-to-A_{1g} Raman modes after exfoliation, followed by UV treatment. However, in the case of exfoliated WS_2 exposed to high-energy β-rays, an anomalous behaviour is observed due to the presence of adequate sulfur vacancies, leading to the disruption of W-S bonds (Fig. 4.2(b)). Additionally, the phonon lifetime (τ) was determined using the uncertainty principle from the acquired Raman spectra, following the equation [16],

$$\frac{1}{\tau} = \frac{\Delta E}{\hbar} = 2\pi c \Gamma \tag{4.2}$$

where ΔE represents the phonon mode energy, c is the speed of light (3×10^8 m/s), Γ denotes the full width at half maximum (FWHM) of the Raman peak (obtained through

multi-peak Lorentzian fitting of the E^1_{2g} and A_{1g} modes), and $\hbar$ is reduced Planck's constant. A comparison of the characteristic phonon lifetimes for pristine and irradiated systems calculated using equation 4.2 is presented in Fig. 4.2(c). The peak positions of the prominent E^1_{2g} and A_{1g} modes, along with their intensity ratio (E^1_{2g}/A_{1g}), FWHM, and phonon lifetime (τ), are summarized in Table 4.1.

Raman spectra were also plotted for bulk WS_2, exfoliated WS_2, and UV- and β-irradiated WS_2 nanosystems, with laser power excitation ranging from 0.25 to 2.5 mW (Fig. 4.3). While variations in vibrational intensities were observed with different laser power excitations, there was no significant peak shift in the studied systems, except for the exfoliated WS_2, which exhibited a redshift in prominent Raman peaks at higher laser excitation (~2.5 mW). Furthermore, mixed or second-order modes, explicitly the $E^1_{2g} + LA$ and $A_{1g} + LA$ modes, which appear as weakly resolved peaks at ~523 cm^{-1} and ~583 cm^{-1}, respectively, were suppressed with increasing laser power in the exfoliated sample as well

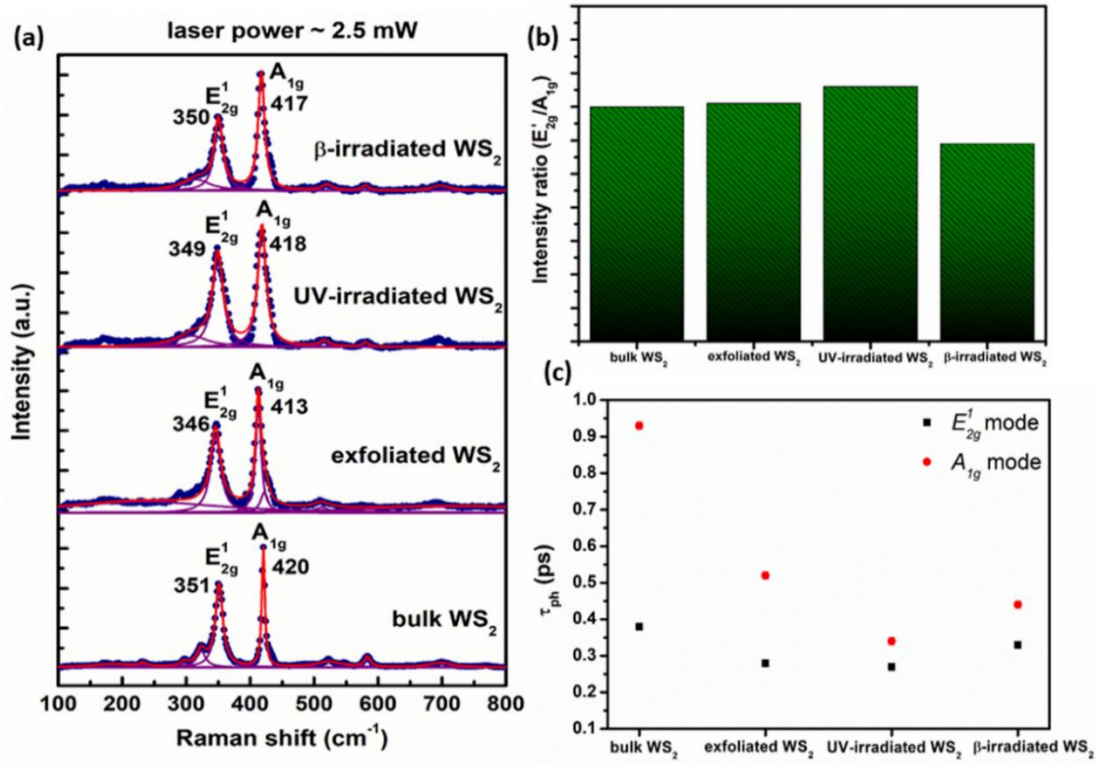

Figure 4.2: (a) Raman spectra, (b) histograms representing the E^1_{2g} to A_{1g} intensity ratio of bulk WS_2, exfoliated WS_2, UV- and β-irradiated WS_2 systems. (c) Plot showing the variations of phonon lifetimes *vs*. vibrational modes of the systems.

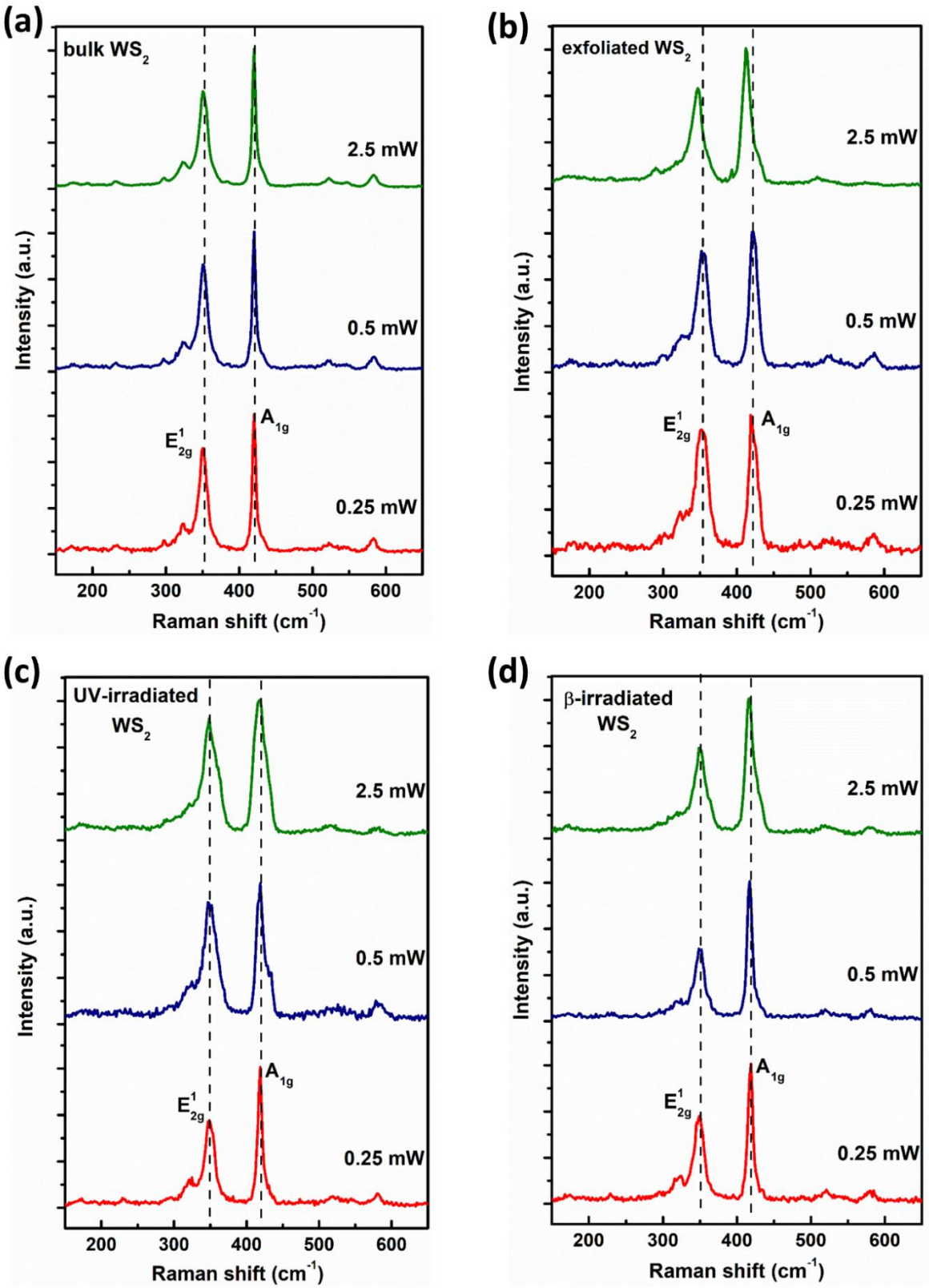

Figure 4.3: Raman spectra of (a) bulk WS_2, (b) exfoliated WS_2, (c) UV- and (d) β-irradiated exfoliated WS_2 nanosystems acquired for different laser powers (~0.25-2.5 mW).

Table 4.1. Raman mode assignment and parameters obtained from the Raman spectra acquired for the laser excitation power of ~2.5 mW.

Sl. No.	Sample	Peak position (cm^{-1})		E^1_{2g}/A_{1g} (intensity ratio)	FWHM modes (cm^{-1})		Phonon lifetime, τ (ps)	
		E^1_{2g} mode	A_{1g} mode		E^1_{2g}	A_{1g}	E^1_{2g} mode	A_{1g} mode
1	Bulk WS_2	351	421	0.70	13.8	5.7	0.4	0.9
2	Exfoliated WS_2	346	413	0.71	18.8	10.2	0.3	0.5
3	UV-irradiated WS_2	349	418	0.76	19.9	15.4	0.3	0.3
4	β-irradiated WS_2	350	417	0.59	16.3	12.0	0.3	0.4

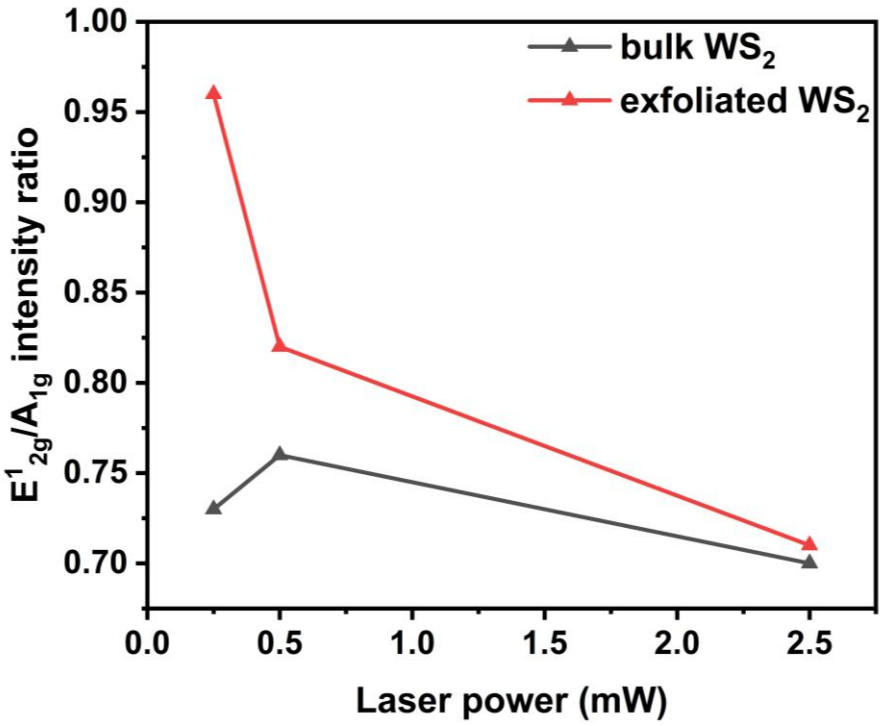

Figure 4.4: Laser power excitation *vs.* E^1_{2g}-*to*-A_{1g} intensity ratio for (a) bulk WS_2 and (b) exfoliated WS_2 nanosheets.

as after UV- and β-irradiation. Additionally, the laser power-dependent Raman observations (~0.25–2.5 mW) concerning the intensity ratio of the E^1_{2g}-to-A_{1g} modes for both bulk and exfoliated WS_2 nanosheets can be found in Fig. 4.4. Notably, the intensity ratio in exfoliated WS_2 is significantly higher than in bulk WS_2, particularly at lower laser power (~0.25 mW). The variations in Raman intensity observed in exfoliated WS_2 with changing laser power can also be attributed to optical interference effects, which are more prominent in thinner layers. In contrast, for bulk WS_2 with a greater number of stacked layers, the Raman laser light has a negligible optical interference effect due to the thickness of the material [17]. However, as the laser power increases, the intensity ratio gradually decreases, aligning with the vibrational characteristics of the bulk system. This behaviour may be attributed to localized heating effects at higher laser powers, which would weaken the atomic bonds [18]. A redshift in the E^1_{2g} mode of the exfoliated system, prominent for laser power excitation of 2.5 mW, as depicted in Fig. 4.3(b), suggests the existence of a microstrain in the system. It is possible that this strain contributes to the noted drop in intensity ratio with increasing laser power [19].

4.6. Nitrogen adsorption/desorption process and pore-size analysis

The adsorption and desorption isotherms measured at liquid nitrogen (N_2) temperature (~77 K) have been analysed to determine the pore-size distribution in bulk WS_2, exfoliated WS_2 and WS_2 system exposed to UV light at an excitation wavelength of ~365 nm for ~30 min and β-rays (delivering a dose of 0.2 kGy). The N_2 adsorption/desorption isotherms and the corresponding pore-size distributions for these systems are presented in Fig. 4.5. The adsorption isotherm follows the principles of gas adsorption, where N_2 molecules are introduced into the system as pressure increases. In contrast, desorption occurs as the pressure is released, often resulting in a hysteresis loop. To be mentioned, pore diameters larger than ~4 nm usually characterize a hysteretic trend [20]. A significant increase in the volume of adsorbed gas at higher relative pressures (p/p_0=0.5-1.0) produces a type-IV isotherm, indicating the presence of a large number of mesopores (dia. 2-50 nm), as shown in Figure 4.5(a). This behaviour is attributed to capillary condensation within these mesopores [21]. As well, the isotherms display a type-H3 hysteresis loop, as classified by IUPAC, suggesting the presence of slit-shaped pores [22] and indicating the absence of limiting adsorption at higher p/p_0 values [23]. Furthermore, as seen in Fig. 4.5(A), the linear segments of the exfoliated and irradiated samples have steeper slopes compared to

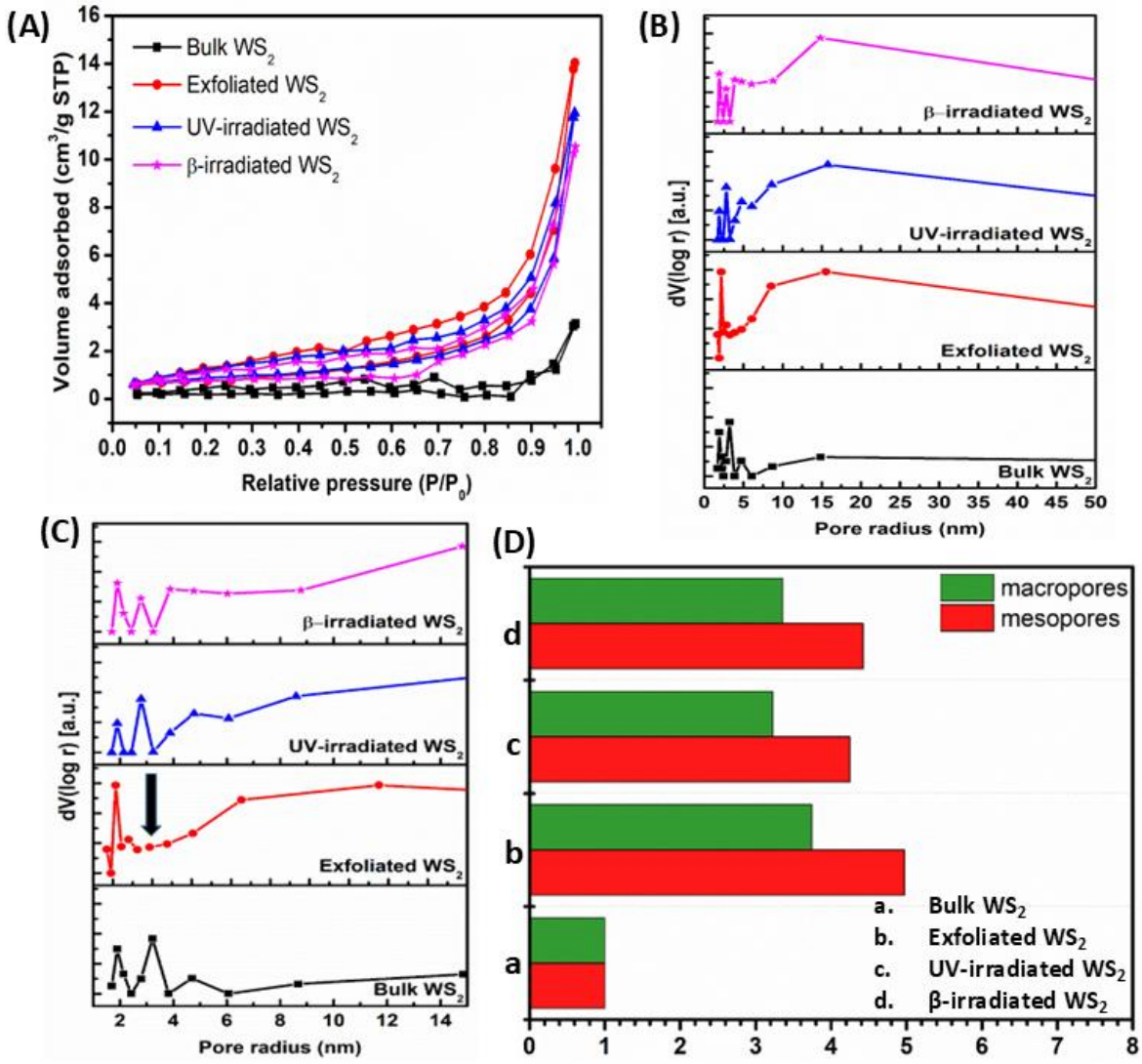

Figure 4.5: (A) N_2 adsorption-desorption isotherms, (B) pore size distribution plots, and (C) zoomed view of pore size distributions of bulk WS_2, exfoliated WS_2, UV- and β-irradiated WS_2, respectively. (D) Comparative bars on meso- and macro-pore size distribution of the specimens considered by comparing the area under the respective curves in the range, d ~8-100 nm.

bulk WS_2, suggesting a rapid yet uniform adsorption/desorption process in the exfoliated, UV-irradiated, and β-irradiated WS_2 systems.

The pore diameters and volume of the porous structures were analysed using the Barrett–Joyner–Halenda (BJH) model [24]. The BJH pore-size distribution graphs for bulk and exfoliated WS_2, and WS_2 systems exposed to UV and β-irradiation are shown in Fig. 4.5 (B,C). The three distinct peaks at ~3.8 nm, 6.4 nm, and 9.4 nm indicate the coexistence of various mesopores in the bulk material, apart from a minimal presence of macropores.

However, in exfoliated WS_2, the absence of the ~6.4 nm peak suggests the formation of new pore sizes, likely due to the shrinking of individual pores or the merging of mesopores into larger ones. This results in a wider range of mesopore size distribution. Interestingly, samples subjected to UV- and β-irradiation exhibit a wider range of pore sizes, spanning from mesopores to macropores, along with the recurrence of the mesopores size of ~6.4 nm. In these irradiated systems, ample mesopores are developed and exhibit greater size variation, while macropores are also present in adequate amounts. This is evident from the area under the curves considered in the range of 8-100 nm (shown in *Appendix* (Fig. A4)), which includes both mesopores (8-50 nm) and macropores (50-100 nm), as illustrated in Fig. 4.5 (D). Notably, the analysis of macropores was limited to pore sizes up to 100 nm due to the lack of sufficient data points beyond this range.

4.7 Congo red dye degradation activity

The photocatalytic degradation efficiency of exfoliated WS_2 and a comparative analysis of exfoliated and irradiated WS_2 systems on congo red (CR) dye under UV light exposure were assessed using UV-vis spectral features. As is known to most chemists and researchers, CR is a water-soluble azo dye that appears as a red colloidal solution, composed of a phenyl ring with two identical halves connected to a naphthalene moiety. It is the sodium salt of benzidine-diazo-bis-1-naphthylamine-4-sulfonic acid, with the chemical formula $C_{32}H_{22}N_6Na_2O_6S_2$. The molecular structure of CR dye is presented in Fig. 4.6. This azo dye, which belongs to the largest class of organic dyestuffs, contains a chromophoric –N=N– azo group [25]. The CR dye exhibits a strong absorbance peak at ~497 nm with a broad spectral feature, primarily absorbing light in the blue region. Under UV light exposure, the dye undergoes rapid degradation through cleavage of the –N=N– bond when exfoliated WS_2 is introduced as a catalyst, exposed up to ~75 min (Fig. 4.7(a)). Additionally, a comparative analysis was conducted for exfoliated WS_2 and UV- and β-irradiated WS_2 catalysts on CR dye over durations of ~15 min and ~45 min, respectively (Fig. 4.7(b, c)). While the exfoliated WS_2 and UV-irradiated WS_2 system displayed inadequate photocatalytic degradation efficiency of only 8.2% and 10.2 % respectively, till 45 min of UV light exposure. Similarly, WS_2 nanostructures showed poor performance, degrading just 15% of the harmful dye even after 105 min [26]. On the other hand, the WS_2 system irradiated with β-rays demonstrated enhanced photocatalytic degradation of CR dye, achieving degradation efficiencies of around 58.6 % and 59.4 % under UV

illumination for ~15 and ~45 min, respectively, as summarized in Table 4.2. This improved performance can be attributed to the presence of varied pores and a relatively higher concentration of sulfur atomic vacancies in the β-irradiated WS_2 system, as revealed by atomic percentage calculations from the EDX spectra. The β-irradiation, a form of ionizing radiation, can deliberately introduce a high number of defects into WS_2 nanocatalyst due to its relatively high energy, significantly greater than that of UV irradiation, which acts in the eV range. These defects can alter the electronic structure of the catalyst or create new active sites, thereby enhancing its catalytic performance [27]. Such structural modifications in the WS_2 catalyst promote the efficient separation and transfer of photo-generated charge carriers while simultaneously reducing the recombination rate of electron-hole pairs. Moreover, sulfur defects are known to enhance the activation of O_2, leading to the generation of more reactive O_2^- and ·OH species [28]. As a result, the overall photocatalytic efficiency of the material is significantly improved. The possible mechanism of the photocatalytic degradation process of CR dye with WS_2 material as a photocatalyst under UV light illumination is presented in Fig. 4.8.

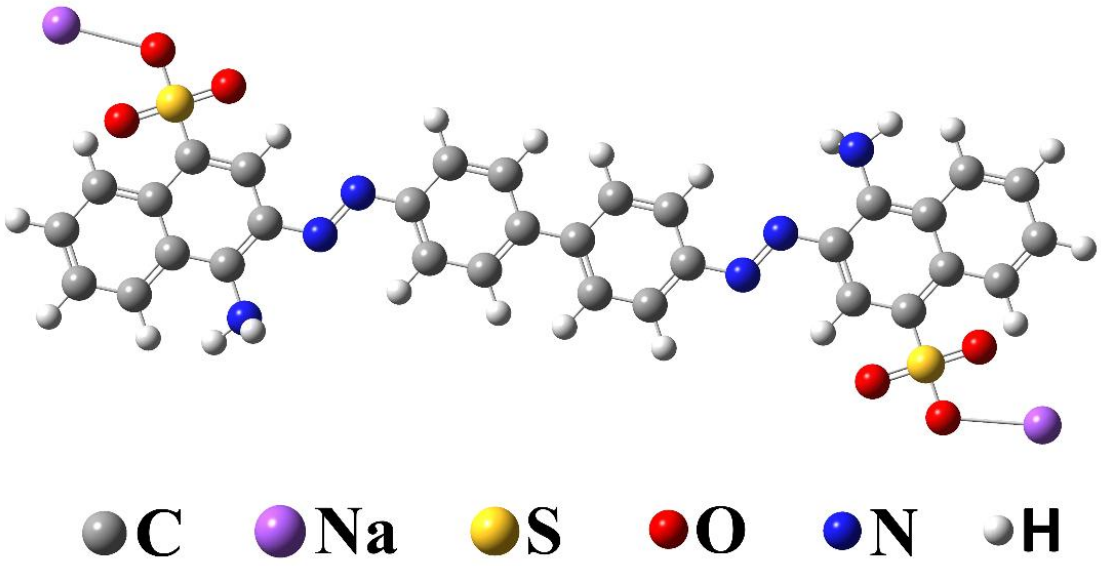

Figure 4.6: The molecular structure of congo red dye in stick-ball configuration.

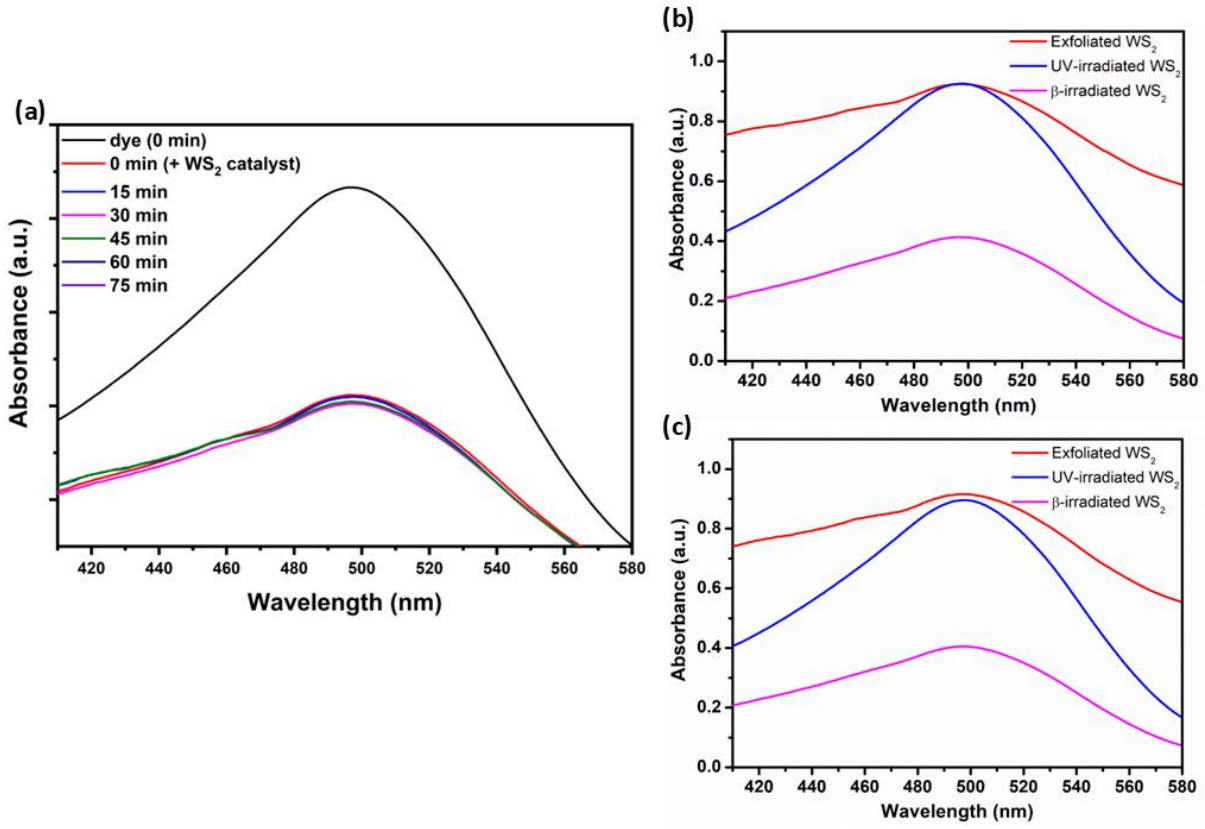

Figure 4.7: (a) Absorbance spectra of congo red (CR) dye added with exfoliated WS_2 until ~75 min exposure. Comparative plot for exfoliated, UV- and β-irradiated WS_2 as a photocatalyst added to CR dye for (b) 15 min, and (c) 45 min, respectively, under UV light exposure.

Table 4.2. Estimation of degradation percentage (%) of congo red dye calculated from the absorbance peak maxima.

Sl. No.	Sample	Degradation (%)	
		15 min illumination	45 min illumination
1	Exfoliated WS_2	07.3	08.2
2	UV-irradiated WS_2	07.3	10.2
3	β-irradiated WS_2	58.6	59.4

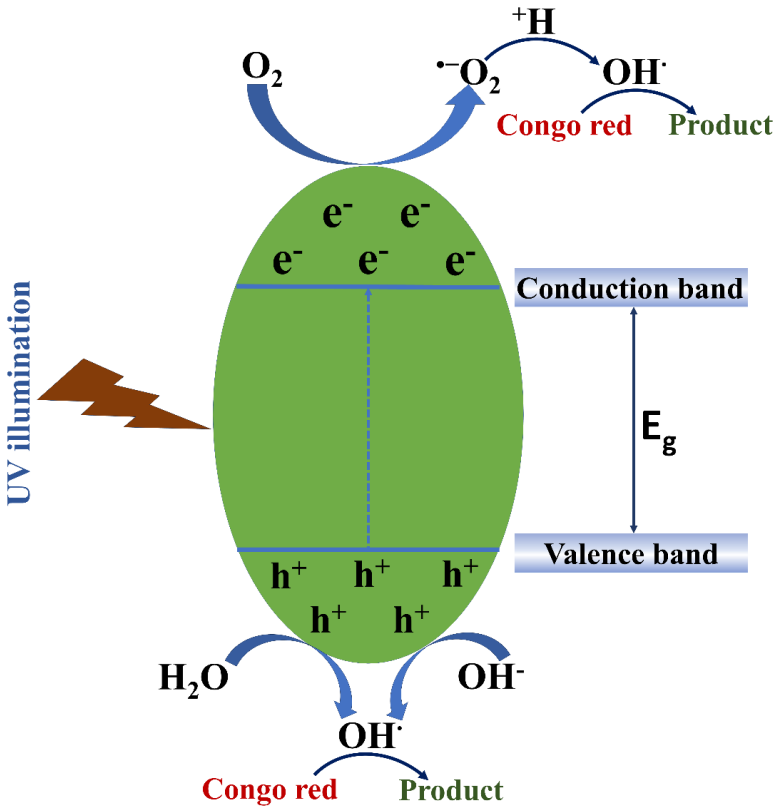

Figure 4.8: Schematic representation of a proposed mechanism of photocatalytic degradation of CR dye with WS_2 nanosystem as a photocatalyst under UV light illumination.

4.8 Concluding remarks

In conclusion, the influence of UV- and β-irradiations on the morphological, vibrational, porosity, and dye degradation activity of the WS_2 system is studied in this chapter. The layered morphology of the WS_2 sheets revealed from FE-SEM imaging envisages the separation of layers from stacks of bulk WS_2 structure. The elemental analysis further confirmed the introduction of sulfur vacancies substantially. Raman spectroscopy was employed to investigate exfoliation in WS_2, with the noticeable E^1_{2g} and A_{1g} vibrational modes, located at ~352 cm^{-1} and ~421 cm^{-1}, respectively, exhibiting redshifts and broadening due to local heating effects with increasing laser power (~2.5 mW). Additionally, an observable increase in the E^1_{2g}-to-A_{1g} intensity ratio in UV-illuminated samples indicates improved exfoliation features under UV exposure. The enrichment of meso-macropores, along with structural defects in the WS_2 nanosheets, is attributed to the exfoliation process and the influence of radiation exposure on the system. Furthermore, the N_2 adsorption-desorption isotherm curve (~77 K) displayed a type-IV characteristic,

confirming the presence of mesopores, while pore-size distribution analysis based on the BJH model revealed the existence of various types of pores in the exfoliated WS_2 as well as after irradiation. A noticeable modification in the distribution of meso-macro pores was observed with radiation. Finally, the photocatalytic degradation efficiency was evaluated using congo red dye, with β-irradiated WS_2 demonstrating an enhanced degradation rate of approx. 59.38% upon UV illumination, for a time dur ation of 45 min.

References

[1] Ali, M.H.H., Goher, M.E., Al-Afify, A.D.G., El-Sayed, S.M. A facile method for synthesis rGO/Ag nanocomposite and its uses for enhancing photocatalytic degradation of Congo red dye. *SN Applied Sciences*, *4*(10): 276, 2022.

[2] Khan, R.R.M., Qamar, H., Hameed, A., Rehman, A.U., Pervaiz, M., Saeed, Z., Adnan, A., Ch, A.R. Biological and Photocatalytic Degradation of Congo Red, a Diazo Sulfonated Substituted Dye: a Review. *Water, Air, & Soil Pollution*, *233*(11): 468, 2022.

[3] Thomas, N., Mathew, S., Nair, K.M., O'Dowd, K., Forouzandeh, P., Goswami, A., McGranaghan, G., Pillai, S.C. 2D MoS_2: structure, mechanisms, and photocatalytic applications. *Materials Today Sustainability*, *13*: 100073, 2021.

[4] Mphahlele, I. J., Malinga, S. P., Dlamini, L. N. A co-doped 2D transition metal dichalcogenide system with the potential of having enhanced photocatalytic properties. *Sustainable Chemistry and Pharmacy*, *24*: 100549, 2021.

[5] Zhao, X., Fu, D., Ding, Z., Zhang, Y.Y., Wan, D., Tan, S.J., Chen, Z., Leng, K., Dan, J., Fu, W., Geng, D. Mo-Terminated Edge Reconstructions in Nanoporous Molybdenum Disulfide Film. *Nano Letters*, *18*(1): 482–490, 2018.

[6] Auret, F. D., Goodman, S. A., Myburg, G., Meyer, W. E. Electrical characterization of defects introduced in n-GaAs by alpha and beta irradiation from radionuclides. *Applied Physics A*, *56*(6): 547–553, 1993.

[7] Wang, H., Liu, X., Niu, P., Wang, S., Shi, J., Li, L. Porous Two-Dimensional Materials for Photocatalytic and Electrocatalytic Applications. *Matter*, *2*(6): 1377–1413, 2020.

[8] Sun, M.H., Huang, S.Z., Chen, L.H., Li, Y., Yang, X.Y., Yuan, Z.Y., Su, B.L. Applications of hierarchically structured porous materials from energy storage and conversion, catalysis, photocatalysis, adsorption, separation, and sensing to biomedicine. *Chemical Society Reviews*, *45*(12): 3479–3563, 2016.

[9] Mohamed, M. G., Atayde, E. C., Matsagar, B. M., Na, J., Yamauchi, Y., Wu, K. C.W., Kuo, S.W. Construction Hierarchically Mesoporous/Microporous Materials Based on Block Copolymer and Covalent Organic Framework. *Journal of the Taiwan Institute of Chemical Engineers*, *112:* 180–192, 2020.

[10] Zeng, X., Ding, Z., Ma, C., Wu, L., Liu, J., Chen, L., Ivey, D.G., Wei, W. Hierarchical Nanocomposite of Hollow N-Doped Carbon Spheres Decorated with Ultrathin WS_2 Nanosheets for High-Performance Lithium-Ion Battery Anode. *ACS Applied Materials & Interfaces*, *8*(29): 18841–18848, 2016.

[11] Su, L., Luo, L., Song, H., Wu, Z., Tu, W., Wang, Z., Ye, J. Hemispherical shell-thin lamellar WS_2 porous structures composited with CdS photocatalysts for enhanced H_2 evolution. *Chemical Engineering Journal*, *388*: 124346, 2020.

[12] Hazarika, S. J., Mohanta, D. Excitation dependent light emission and enhanced photocatalytic response of WS_2/C-dot hybrid nanoscale systems. *Journal of Luminescence*, *206*: 530–539, 2019.

[13] Juget, F., Nedjadi, Y., Buchillier, T., Bochud, F., Bailat, C. Determination of ^{137}Cs half-life with an ionization chamber. *Applied Radiation and Isotopes*, *118*: 215–220, 2016.

[14] Sen, S., Das, C., Ghosh, N.N., Baildya, N., Bhattacharya, S., Khan, M.A., Sillanpää, M., Biswas, G. Is degradation of dyes even possible without using photocatalysts? – a detailed comparative study. *RSC Advances*, *12*(53): 34335–34345, 2022.

[15] Sourisseau, C., Fouassier, M., Alba, M., Ghorayeb, A., Gorochov, O. Resonance Raman, inelastic neutron scattering and lattice dynamics studies of 2H-WS_2. *Materials Science and Engineering: B*, *3*(1): 119–123, 1989.

[16] Cuscó, R., Alarcón-Lladó, E., Ibáñez, J., Artús, L., Jiménez, J., Wang, B., Callahan, M. J. Temperature dependence of Raman scattering in ZnO. *Physical Review B*, *75*(16): 165202, 2007.

[17] Zobeiri, H., Xu, S., Yue, Y., Zhang, Q., Xie, Y., Wang, X. Effect of temperature on Raman intensity of nm-thick WS_2: combined effects of resonance Raman, optical properties, and interface optical interference. *Nanoscale*, *12*(10): 6064–6078, 2020.

[18] Sahoo, S., Gaur, A. P. S., Ahmadi, M., Guinel, M. J.-F., Katiyar, R. S. Temperature-Dependent Raman Studies and Thermal Conductivity of Few-Layer MoS_2. *The Journal of Physical Chemistry C*, *117*(17): 9042–9047, 2013.

[19] Dadgar, A.M., Scullion, D., Kang, K., Esposito, D., Yang, E.H., Herman, I.P., Pimenta, M.A., Santos, E.J., Pasupathy, A.N. Strain Engineering and Raman Spectroscopy of Monolayer Transition Metal Dichalcogenides. *Chemistry of Materials*, *30*(15): 5148–5155, 2018.

[20] Akple, M. S., Low, J., Wageh, S., Al-Ghamdi, Ahmed. A., Yu, J., Zhang, J. Enhanced visible light photocatalytic H_2-production of g-C_3N_4/WS_2 composite heterostructures. *Applied Surface Science*, *358*: 196–203, 2015.

[21] Dutta, N., Mohanta, D., Choudhury, A. Synthesis and pore filling mechanism in anatase TiO_2 nanostructured network mediated by PbS molecular adsorption. *Journal of Applied Physics*, *109*(9): 094904, 2011.

[22] Sing, K. S. W. Reporting physisorption data for gas/solid systems with special reference to the determination of surface area and porosity (Recommendations 1984), *57*(4): 603–619, 1985.

[23] Thommes, M., Smarsly, B., Groenewolt, M., Ravikovitch, P. I., Neimark, A. V. Adsorption Hysteresis of Nitrogen and Argon in Pore Networks and Characterization of Novel Micro- and Mesoporous Silicas. *Langmuir*, *22*(2): 756–764, 2006.

[24] Barrett, E. P., Joyner, L. G., Halenda, P. P. The Determination of Pore Volume and Area Distributions in Porous Substances. I. Computations from Nitrogen Isotherms. *Journal of the American Chemical Society*, *73*(1): 373–380, 1951.

[25] Khan, R.R.M., Qamar, H., Hameed, A., Rehman, A.U., Pervaiz, M., Saeed, Z., Adnan, A., Ch, A.R. Biological and Photocatalytic Degradation of Congo Red, a Diazo Sulfonated Substituted Dye: a Review. *Water, Air, & Soil Pollution*, *233*(11): 468, 2022.

[26] Joseph, A., Aneesh, P. M. Efficient degradation of methylene blue: A comparative study using hydrothermally synthesised SnS_2, WS_2 and VS_2 nanostructures. *Materials Research Bulletin*, *146*: 111623, 2022.

[27] Huang, S., Yue, C., Uvdal, K., Hu, Z. Recent advances in irradiation-mediated synthesis and tailoring of inorganic nanomaterials for photo-/electrocatalysis. *Nanoscale Advances*, *7*(2): 384–418, 2025.

[28] Cai, J., Xia, Y., Gang, R., He, S., Komarneni, S. Activation of MoS_2 via tungsten doping for efficient photocatalytic oxidation of gaseous mercury. *Applied Catalysis B: Environmental*, *314*: 121486, 2022.